

Ultrafast Ultrasound Imaging With Cascaded Dual-Polarity Waves

Yang Zhang, *Student Member, IEEE*, Yuexin Guo, *Student Member, IEEE*,
and Wei-Ning Lee[✉], *Member, IEEE*

Abstract—Ultrafast ultrasound imaging using plane or diverging waves, instead of focused beams, has advanced greatly the development of novel ultrasound imaging methods for evaluating tissue functions beyond anatomical information. However, the sonographic signal-to-noise ratio (SNR) of ultrafast imaging remains limited due to the lack of transmission focusing, and thus insufficient acoustic energy delivery. We hereby propose a new **ultrafast ultrasound imaging methodology with cascaded dual-polarity waves (CDWs), which consists of a pulse train with positive and negative polarities**. A new coding scheme and a corresponding linear decoding process were thereby designed to obtain the recovered signals with increased amplitude, thus increasing the SNR without sacrificing the frame rate. The newly designed CDW ultrafast ultrasound imaging technique achieved higher quality B-mode images than coherent plane-wave compounding (CPWC) and multiplane wave (MW) imaging in a calibration phantom, *ex vivo* pork belly, and *in vivo* human back muscle. CDW imaging shows a significant **improvement in the SNR (10.71 dB versus CPWC and 7.62 dB versus MW)**, **penetration depth (36.94% versus CPWC and 35.14% versus MW)**, and **contrast ratio in deep regions (5.97 dB versus CPWC and 5.05 dB versus MW) without compromising other image quality metrics**, such as spatial resolution and frame rate. The enhanced image qualities and ultrafast frame rates offered by CDW imaging beget great potential for various novel imaging applications.

Index Terms—Coding scheme, plane wave, polarity, signal-to-noise ratio, ultrafast, ultrasound.

I. INTRODUCTION

ULTRAFAST imaging using plane waves or diverging waves, instead of the focused beams, is a paradigm shift for biomedical ultrasound imaging from real-time acquisitions (tens of frames per second (fps)) to the ultrafast category (thousands fps) [1]. It emboldens the development of novel ultrasound imaging methods for evaluating tissue functions beyond anatomical information, such as shear wave elastography [2]–[5], ultrafast Doppler imaging [6]–[8], contrast agent

dynamics [9], [10], myocardial strain imaging [11]–[13], and parametric imaging [14].

Originally, the ultrafast imaging system was based on a flat plane-wave transmission [15], [16]. In [15], an ultrafast imaging system (up to 10,000 frames/s) was developed with a flat plane-wave illumination and parallel beamforming techniques to track a low-frequency (200 Hz) transient shear wave propagation in gel-based phantoms. A plane-wave transmission with limited diffraction beam reception was proposed [16], [17] to reconstruct two-dimensional (2D) and three-dimensional (3D) images in the Fourier domain with a frame rate up to 3,750 fps for biological tissues at a depth of 200 mm. The frame rate of the flat plane-wave-based imaging can reach the physical limits of medical ultrasound imaging, but the resultant image quality in terms of resolution, contrast, and signal-to-noise ratio (SNR) was much more degraded than that of conventional focused imaging because of the lack of transmit focus [1].

Thereafter, coherent plane-wave compounding (CPWC), which exploited a coherent recombination of tilted plane-wave transmissions, was proposed [18], [19] to obtain images with equivalent spatial resolution, contrast, and SNR to conventional multi-focus imaging while preserving the high frame-rate capabilities. Similarly, coherent compounding of full aperture diverging waves [20], [21] and subaperture diverging waves [22] (CDWC) were further developed for high frame-rate cardiac imaging. Instead of diverging waves, multi-transmit beamforming methods were proposed in [23] to increase the frame rate of cardiac imaging, in which multiple focused beams were transmitted simultaneously. A tradeoff between the image quality and the frame rate in coherent compounding techniques was balanced by the flexible selection of the compounded tilted plane waves or diverging waves. For example, two to five waves are typically used for transient shear wave elastography to ensure a compounded frame rate higher than 1 kHz because the typical spectrum of interest of shear waves propagating in the human body is of few hundred Hz [2]. At such a high frame rate, image contrast and SNR are compromised, and the use of plane wave transmissions lead to the known inherent axial lobe artifact. We therefore recently developed a new ultrafast imaging technique with combined transmissions and coherence-based reconstruction to reduce the axial lobe and side lobe artifacts to enhance the ultrafast image contrast [24].

However, the ultrafast image SNR remains limited due to the few number of unfocused wave transmissions. Both the frame rate and SNR are valuable for medical ultrasound imag-

Manuscript received September 2, 2017; revised November 23, 2017; accepted November 27, 2017. Date of publication December 8, 2017; date of current version April 2, 2018. This work was supported in part by the Hong Kong Research Grants Council under Grant ECS 739413E and in part by the University Development Fund. (Corresponding author: Wei-Ning Lee.)

Y. Zhang and Y. Guo are with the Department of Electrical and Electronic Engineering, The University of Hong Kong, Hong Kong.

W.-N. Lee is with the Department of Electrical and Electronic Engineering, The University of Hong Kong, Hong Kong, and also with the Medical Engineering Programme (e-mail: wnlee@eee.hku.hk).

Color versions of one or more of the figures in this paper are available online at <http://ieeexplore.ieee.org>.

Digital Object Identifier 10.1109/TMI.2017.2781261

ing. Higher SNR enables deep tissue imaging and increases the sensitivity and accuracy for mapping tissue functions beyond anatomical information. In addition, higher SNR also enables the use of higher frequencies, together yielding images with better resolution and contrast. Due to the safety issues of the medical ultrasound imaging, the maximum allowable Mechanical Index (MI) limits the maximum amplitude of the transmitted signals. Therefore, how to increase the SNR without changing the amplitude of the transmitted signals needs to be investigated. Several coded excitation techniques were investigated to increase the SNR of ultrasound imaging [25]–[28]. Conventional coded excitation techniques, such as Chirp and Golay code [25], [29]–[31] could increase the SNR of medical ultrasound imaging. For the Chirp and Golay excitations, long modulated signals, instead of a short pulse, are transmitted, and the received signals are decoded by the correspondingly designed pulse compression filter. However, the decoding of chirp signals requires a priori knowledge of the signal propagation properties of the medium, such as the attenuation, to design the pulse compression filter. The application of Golay code in ultrasound imaging leads to a reduction of the frame rate by a factor of 2, which is not desirable in ultrafast imaging. In addition, coded excitation techniques with orthogonal frequency division multiplexing and parallel transmit beamforming was combined on an ultrasound scanner in [31] to overcome the inter-beam interference shortcomings. Recently, a multiplane wave (MW) imaging method using Hadamard encoding was proposed [32] to increase the SNR of ultrafast imaging without compromising the frame rate. Unlike conventional coded excitation techniques, by which long modulated signals are transmitted and the received signals are decoded by the designed pulse compression filter, MW imaging transmits successively multiple tilted plane waves encoded by a Hadamard matrix with a short time interval for each transmission-acquisition event. The high-intensity signals from each tilted plane-wave transmission can be decoded from the received signals in different transmission-acquisition events. The decoding process simply relies on addition and subtraction operations without a cumbersome pulse compression filter design. MW improves the SNR by $10 \cdot \log_{10}(M)$ when M steering angles and acquisitions are used. MW imaging has been demonstrated to yield accurate elasticity maps with a smaller variance for shear wave elastography [32] and detect deeper blood signals in ultrafast Doppler imaging compared with CPWC [32]. MW imaging has further been combined with the delay-encoded harmonic imaging to improve both the SNR and resolution of ultrafast images [33]. Nonetheless, SNR improvement is limited to the number of compounded tilted plane waves or diverging waves. For example, the improvement of SNR is only 3 dB for shear wave elastography with two compounded tilted plane waves to ensure the ultrafast frame rates. In addition, the number of compounded tilted plane waves is bound to $M = 2^m$, where m is an integer. One remaining challenge to tackle is greater SNR improvement in ultrafast imaging with as few compounded transmissions as possible.

In this study, we propose a new coding matrix whose length is longer than the square Hadamard matrix of order 2 and

apply the newly designed coding matrix to medical ultrasound imaging. The new ultrafast ultrasound imaging method herein is coined as “Cascaded Dual-polarity Waves (CDW) Imaging” for increasing SNR and sensitivity in ultrafast imaging with few compounded transmissions. The newly designed CDW code is a $2 \times N$ matrix with two polarities: $+1$ and -1 , and $N = 2^k$, where k is an integer. Based on the newly designed CDW code, N cascaded dual-polarity waves are transmitted for each reception, unlike one single wave in conventional CPWC. The corresponding decoding process consists of addition, subtraction, and delay operations. It is hence as simple as that of the Hadamard code but gains a sonographic SNR of $10 \cdot \log_{10}(N)$. In addition to medical ultrasound imaging, the CDW imaging may have a potential to improve the SNR of other array-based imaging modalities, such as microwave imaging.

II. THEORY

A theoretical framework is introduced to explain the different signal models for transmission and reception in the array-based medical imaging scenarios. In the signal models, $x(t)$ represents the transmitted signals (a matrix of signals from each activated array element) by the array with full-aperture or sub-aperture transmission. The transmitted signals will propagate and interact with soft tissues, and backscattered signals $y(t)$ are recorded by the array with full aperture for each transmission-reception event.

A. Conventional Single-Wave Model

In conventional single wave transmission, the signals for each pair of successive transmissions are given by

$$\begin{cases} x_1(t) = a_1 \cdot s_1(t) \\ x_2(t) = a_2 \cdot s_2(t), \end{cases} \quad (1)$$

where $s_1(t)$ and $s_2(t)$ represent the source signals, and a_1 and a_2 represent the coefficients of the signals with a given value of -1 or $+1$. Suppose that $h(t)$ is the impulse response of the wave propagation channel. From each transmission, the noise-free received signals can be described by

$$\begin{cases} y_1(t) = a_1 \cdot s_1(t) * h(t) \\ y_2(t) = a_2 \cdot s_2(t) * h(t), \end{cases} \quad (2)$$

where $*$ denote the convolution operation. The received signals $y_1(t)$ and $y_2(t)$ typically have much smaller amplitudes than the transmitted signals because of attenuation and scattering effects of the medium. In addition, the amplitude of the transmitted signals and thus the transmit voltage allowed are regulated by the FDA safety guidelines. Thus, conventional single wave transmissions suffer from limited SNR and penetration depth in medical imaging.

B. Multiplane Wave Model With Hadamard Matrix

In order to obtain the received signals with increased amplitude without an increase in the amplitude or the number of transmissions, multiple coded waves are utilized [32]. The Hadamard encoding scheme is the starting point of this

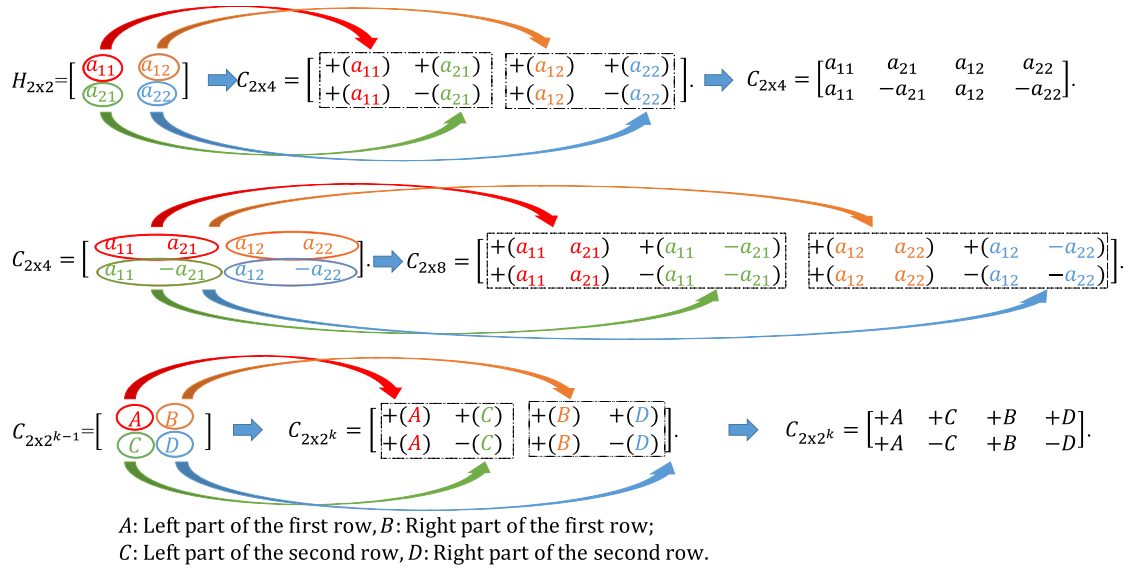


Fig. 1. Illustration of the design of the proposed CDW coding matrix.

scenario, in which the signals for each pair of successive transmissions are given by

$$\begin{cases} x_{h1}(t) = a_{11} \cdot s_1(t) + a_{12} \cdot s_2(t) * \delta(t - \tau) \\ x_{h2}(t) = a_{21} \cdot s_1(t) + a_{22} \cdot s_2(t) * \delta(t - \tau), \end{cases} \quad (3)$$

where $x_{h1}(t)$ is the first transmission, $x_{h2}(t)$ is the second transmission, τ is the preset delay added between the first wave $s_1(t)$ and the second wave $s_2(t)$, and $a_{11}, a_{12}, a_{21}, a_{22}$ are the values of the Hadamard matrix of order 2 [34], which is given by

$$H_{2 \times 2} = \begin{bmatrix} a_{11} & a_{12} \\ a_{21} & a_{22} \end{bmatrix} = \begin{bmatrix} 1 & 1 \\ 1 & -1 \end{bmatrix}. \quad (4)$$

Then, the received signals from each transmission can be written as

$$\begin{cases} y_{h1}(t) = s_1(t) * h(t) + s_2(t) * \delta(t - \tau) * h(t) \\ y_{h2}(t) = s_1(t) * h(t) - s_2(t) * \delta(t - \tau) * h(t). \end{cases} \quad (5)$$

The received signals with a 2-fold amplitude increase can be retrieved based on simple linear decoding as follows:

$$\begin{cases} y'_{h1}(t) = y_{h1}(t) + y_{h2}(t) = 2 \cdot s_1(t) * h(t) \\ y'_{h2}(t) = y_{h1}(t) - y_{h2}(t) = 2 \cdot s_2(t) * \delta(t - \tau) * h(t). \end{cases} \quad (6)$$

Since the delay τ is known, the second received signal, $y'_{h2}(t)$, can be compensated as follows:

$$y''_{h2}(t) = y'_{h2}(t) * \delta(t + \tau) = 2 \cdot s_2(t) * h(t). \quad (7)$$

Equations (6) and (7) show that amplitudes of the recovered received signals $y'_{h1}(t)$ and $y''_{h2}(t)$ are increased by 2 fold compared with $y_1(t)$ and $y_2(t)$ in the single wave transmission. This increase in the amplitude leads to an increased SNR and penetration depth for medical imaging.

C. Proposed Cascaded Dual-Polarity Waves Model

Inspired by the multiplane wave model with Hadamard matrix, we propose a cascaded dual-polarity waves (CDW) scheme to further elevate the SNR of the recovered received signals.

Although the Hadamard matrix can increase the SNR of the recovered received signals, the improvement is limited to the order of the matrix (i.e. only two times for each pair of transmissions). Our proposed CDW coding and decoding scheme makes use of cascaded wave transmissions to profoundly improve the SNR of the recovered received signals. In the CDW scheme, each transmitted signal contains N ($N = 2^k, k = 0, 1, 2, \dots$) waves to gain SNR of $10 \cdot \log_{10}(N)$ on the energy. The signals for each pair of the successive transmissions are given by

$$\begin{cases} x_{s1}(t) = \sum_{i=1}^{2^{k-1}} a_{1i} \cdot s_1(t) * \delta(t - (i-1) \cdot \tau) \\ \quad + \sum_{i=2^{k-1}+1}^N a_{1i} \cdot s_2(t) * \delta(t - (i-1) \cdot \tau) \\ x_{s2}(t) = \sum_{i=1}^{2^{k-1}} a_{2i} \cdot s_1(t) * \delta(t - (i-1) \cdot \tau) \\ \quad + \sum_{i=2^{k-1}+1}^N a_{2i} \cdot s_2(t) * \delta(t - (i-1) \cdot \tau), \end{cases} \quad (8)$$

Note that each set of N waves contains two source signals, $s_1(t)$ and $s_2(t)$, with preset delays and different polarities or phase coefficients which are determined by our newly designed CDW coding matrix.

Let's consider a four-wave ($N = 4$) model as illustrated in Fig. 1. For $N = 2$, the CDW coding matrix is the same as the Hadamard matrix of order 2 ($H_{2 \times 2}$), from which the 2×4 CDW matrix can be designed in following steps:

- 1) A 2-by-4 matrix is first written by repeating $H_{2 \times 2}$:

$$C'_{2 \times 4} = [H_{2 \times 2} H_{2 \times 2}] = \begin{bmatrix} +1 & +1 & +1 & +1 \\ +1 & -1 & +1 & -1 \end{bmatrix}, \quad (9)$$

where the third and the fourth columns are simply a duplicate of the first and second columns of $H_{2 \times 2}$, respectively. This step sets the default sign of $C_{2 \times 4}''$.

- 2) Another 2-by-4 matrix is created by taking each element from $H_{2 \times 2}$ and its replica to form a column vector and then concatenating the four column vectors:

$$C_{2 \times 4}'' = \begin{bmatrix} a_{11} & a_{21} & a_{12} & a_{22} \\ a_{11} & a_{21} & a_{12} & a_{22} \end{bmatrix}. \quad (10)$$

- 3) The final 2-by-4 CDW matrix is obtained by the element-wise multiplication of $C_{2 \times 4}'$ and $C_{2 \times 4}''$ as

$$\begin{aligned} C_{2 \times 4} &= C_{2 \times 4}' * C_{2 \times 4}'' = \begin{bmatrix} a_{11} & a_{21} & a_{12} & a_{22} \\ a_{11} & -a_{21} & a_{12} & -a_{22} \end{bmatrix} \\ &= \begin{bmatrix} 1 & 1 & 1 & -1 \\ 1 & -1 & 1 & 1 \end{bmatrix}. \end{aligned} \quad (11)$$

where $a_{11} = a_{12} = a_{21} = 1$, $a_{22} = -1$, and $*$ denotes the element-by-element multiplication of two matrices. The first and second rows in $C_{2 \times 4}$ represent the first and second transmissions, respectively. Each transmission is comprised of four waves.

The signals for each pair of successive transmissions with four waves can therefore be formulated as

$$\begin{cases} x_{s1}(t) = s_1(t) + s_1(t) * \delta(t - \tau) \\ \quad + s_2(t) * \delta(t - 2\tau) - s_2(t) * \delta(t - 3\tau) \\ x_{s2}(t) = s_1(t) - s_1(t) * \delta(t - \tau) \\ \quad + s_2(t) * \delta(t - 2\tau) + s_2(t) * \delta(t - 3\tau). \end{cases} \quad (12)$$

Then, the received signals will be

$$\begin{cases} y_{s1}(t) = s_1(t) * h(t) + s_1(t) * \delta(t - \tau) * h(t) \\ \quad + s_2(t) * \delta(t - 2\tau) * h(t) - s_2(t) * \delta(t - 3\tau) * h(t) \\ y_{s2}(t) = s_1(t) * h(t) - s_1(t) * \delta(t - \tau) * h(t) \\ \quad + s_2(t) * \delta(t - 2\tau) * h(t) + s_2(t) * \delta(t - 3\tau) * h(t). \end{cases} \quad (13)$$

Following the reception of backscattered signals, a linear decoding process is designed based on addition, subtraction and delay operations as follows:

- 1) The received signals from the paired transmissions are summed and subtracted to obtain

$$\begin{cases} y_{s1}'(t) = y_{s1}(t) + y_{s2}(t) \\ \quad = 2 \cdot s_1(t) * h(t) + 2 \cdot s_2(t) * \delta(t - 2\tau) * h(t) \\ y_{s2}'(t) = y_{s1}(t) - y_{s2}(t) \\ \quad = 2 \cdot s_1(t) * \delta(t - \tau) * h(t) - 2 \cdot s_2(t) * \delta(t - 3\tau) * h(t). \end{cases} \quad (14)$$

- 2) $y_{s2}'(t)$ can be compensated by the delay operation to obtain

$$\begin{aligned} y_{s2}''(t) &= y_{s2}'(t) * \delta(t + \tau) \\ &= 2 \cdot s_1(t) * h(t) - 2 \cdot s_2(t) * \delta(t - 2\tau) * h(t). \end{aligned} \quad (15)$$

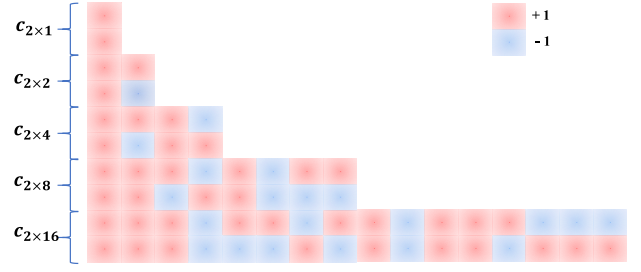


Fig. 2. Designed CDW coding matrix with a length of 1, 2, 4, 8, and 16.

- 3) $y_{s1}'(t)$ and $y_{s2}''(t)$ are summed or subtracted to obtain

$$\begin{cases} y_{s1}''(t) = y_{s1}'(t) + y_{s2}''(t) = 4 \cdot s_1(t) * h(t) \\ y_{s2}'''(t) = y_{s1}'(t) - y_{s2}''(t) = 4 \cdot s_2(t) * \delta(t - 2\tau) * h(t). \end{cases} \quad (16)$$

- 4) $y_{s2}'''(t)$ can similarly be compensated by the delay operation to obtain

$$y_{s2}''''(t) = y_{s2}'''(t) * \delta(t + 2\tau) = 4 \cdot s_2(t) * h(t). \quad (17)$$

- 5) The final decoded signals with high amplitude will be

$$\begin{cases} y_{s1}''(t) = 4 \cdot s_1(t) * h(t) = 4 \cdot y_1(t) \\ y_{s2}''''(t) = 4 \cdot s_2(t) * h(t) = 4 \cdot y_2(t). \end{cases} \quad (18)$$

The amplitudes of the recovered received signals $y_{s1}''(t)$ and $y_{s2}''''(t)$ are four times higher than those of $y_1(t)$ and $y_2(t)$ by single wave transmissions.

Similar to the $C_{2 \times 4}$ CDW matrix derived from the $H_{2 \times 2}$ Hadamard matrix, the $C_{2 \times 8}$ CDW matrix can be obtained with the described coding procedure from the $C_{2 \times 4}$ CDW matrix as shown in Fig. 1. The difference is that the elements in the first and the second rows of the $C_{2 \times 4}$ CDW matrix are first divided into the left and right parts, respectively. Then, we have

$$\begin{aligned} C_{2 \times 8} &= \begin{bmatrix} a_{11} & a_{21} & a_{11} & -a_{21} & a_{12} & a_{22} & a_{12} & -a_{22} \\ a_{11} & a_{21} & -a_{11} & a_{21} & a_{12} & a_{22} & -a_{12} & a_{22} \end{bmatrix} \\ &= \begin{bmatrix} +1 & +1 & +1 & -1 & +1 & -1 & +1 & +1 \\ +1 & +1 & -1 & +1 & +1 & -1 & -1 & -1 \end{bmatrix}. \end{aligned} \quad (19)$$

In addition, a $C_{2 \times 16}$ CDW matrix can be obtained from the $C_{2 \times 8}$ CDW matrix, and so on. In general, a $C_{2 \times 2^k}$ CDW matrix can be derived from the $C_{2 \times 2^{k-1}}$ CDW matrix with the similar coding procedure as shown in Fig. 1, where A represents the block matrix consisting of the left part of the first row, B represents the block matrix consisting of the right part of the first row, C represents the block matrix consisting of the left part of the second row, and D represents the block matrix consisting of the right part of the second row. Figure 2 shows the designed CDW matrix with a length of 2^k , where k is an integer. This entire encoding procedure thus gives the name of our proposed method—cascaded dual-polarity waves.

Figure 3 shows the general decoding process. The decoder consists of addition, subtraction, and delay operations. In the

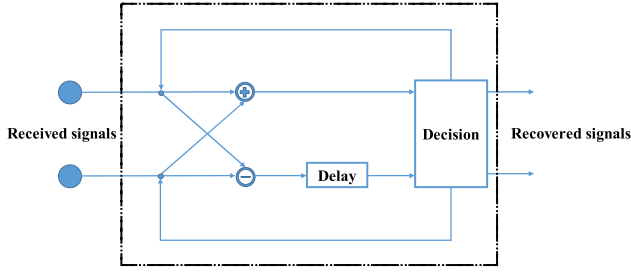


Fig. 3. The proposed decoding process for the CDW coding matrix.

first loop, the received signals from two successive transmissions are summed or subtracted and then delayed to obtain the processed signals. The decider is used to send the processed signals for the next loop or the final decoded output signals. The number of the loops is $L = \log_2(N)$ with N waves, and the delay for the l -th loop is

$$\tau_l = \begin{cases} N/(2^{l+1}) * \tau, & 0 < l < L \\ (N/2) * \tau, & l = L. \end{cases} \quad (20)$$

Moreover, the described CDW coding and decoding theory can also be applied to M transmits, in which each of the two successive transmits could be processed based on the $C_{2 \times N}$ CDW matrix.

III. METHODS

The application of the designed CDW coding and decoding scheme to medical ultrasound imaging is introduced.

A. Imaging Sequence Design With Cascaded Dual-Polarity Waves

The CDW imaging sequence design is inspired by the CPWC imaging [18], [19] and MW imaging [32], and it consists of the transmission and reception parts. In transmission, each transmitted signal is a long pulse which contains N ($N = 2^k$, $k = 0, 1, 2, \dots$) cascaded waves with short time intervals and $+1$ or -1 polarity coefficients, instead of the conventional short pulse with a single wave. In reception, a linear decoding scheme comprised of addition, subtraction, and delay operations is devised to recover N times higher intensity backscattered signals to gain SNR of $10 \cdot \log_{10}(N)$.

The type of the wave in CDW imaging can be the plane wave, diverging wave, focused wave, or other forms. A flat planar wavefront is generated by simultaneously activating all the elements in the array, and a tilted planar wavefront is generated by sequentially activating the elements in the array. A diverging wave can be generated by setting a virtual source behind the array. A focused wave can be generated by setting a focus in front of the array. In this study, we use plane wave as an example to elucidate the sequence design of CDW imaging.

Figure 4 shows the two-transmit sequence of our proposed CDW imaging with eight cascaded waves for each transmission. The diagram of the initially transmitted cascaded waves is shown in Fig. 4(a). In transmission, each transmitted signal is a long pulse which contains eight cascaded waves with short time intervals and $+1$ or -1 polarity coefficients. The 1st to 4th

waves are tilted plane waves with a steering angle of θ_1 , and the 5th to 8th waves are tilted plane waves with a steering angle of θ_2 . The polarity coefficients are obtained from the designed CDW matrix in Section II. The polarity of the first transmit event T1 is $[+1, +1, +1, -1, +1, -1, +1, +1]$, and the second transmit event T2 is $[+1, +1, -1, +1, +1, -1, -1, -1]$.

In reception, received signals from each transmit event are acquired and called R1 and R2 signals. Figures 4(b)-(g) show the decoding process described in Section II to recover eight-times higher signals from the initially acquired signals. In our study, full aperture of the array was deployed to receive the backscattered signals. The received R1 or R2 signals of the array by each transmit-reception event was a two-dimensional (2D) matrix with N_s rows and 128 columns, where N_s was the number of samples of the received signal by each element, and 128 was the number of array elements. The addition, subtraction, and delay operations in the decoding process were directly implemented on the 2D matrix of received signals (i.e., channel data) before the beamforming process. The detailed decoding process can be explained as follows:

- 1) R1 and R2 signals with two-fold amplitude in Fig. 4(b) are obtained by the addition and subtraction of the initial R1 and R2 signals in Fig. 4(a), respectively. The coefficients of R1 and R2 in Fig. 4(b) are $[+2, +2, 0, 0, +2, -2, 0, 0]$ and $[0, 0, +2, -2, 0, 0, +2, +2]$.
- 2) The R2 signal in Fig. 4(b) is delayed to obtain the R2 signal in Fig. 4(c). The coefficients of R1 and R2 in Fig. 4(c) are $[+2, +2, 0, 0, +2, -2, 0, 0]$ and $[+2, -2, 0, 0, +2, +2, 0, 0]$.
- 3) Similar to the step (1), R1 and R2 signals with four-fold amplitude in Fig. 4(d) are obtained by the addition and subtraction of the R1 and R2 signals in Fig. 4(c). The coefficients of R1 and R2 in Fig. 4(d) are $[+4, 0, 0, 0, +4, 0, 0, 0]$ and $[0, +4, 0, 0, 0, -4, 0, 0]$.
- 4) Similar to the step (2), the R2 signal in Fig. 4(d) is delayed to obtain the R2 signal in Fig. 4(e). The coefficients of R1 and R2 in Fig. 4(e) are $[+4, 0, 0, 0, +4, 0, 0, 0]$ and $[+4, 0, 0, 0, -4, 0, 0, 0]$.
- 5) Similar to the step (3), R1 and R2 signals with eight-fold amplitude in Fig. 4(f) are obtained by the addition and subtraction of the R1 and R2 signals in Fig. 4(e). The coefficients of R1 and R2 in Fig. 4(f) are $[+8, 0, 0, 0, 0, 0, 0, 0]$ and $[0, 0, 0, 0, +8, 0, 0, 0]$.
- 6) Similar to the step (4), the R2 signal in Fig. 4(f) is delayed to obtain the R2 signal in Fig. 4(g). The coefficients of R1 and R2 in Fig. 4(g) are $[+8, 0, 0, 0, 0, 0, 0, 0]$ and $[+8, 0, 0, 0, 0, 0, 0, 0]$, each of which is equivalent to the 8-fold amplitude of the single wave transmission.

The two-transmit sequence can be extended to the M -transmit sequence. Such extension is similar to CPWC with M steering angles, where M is an even number and $M > 2$. Each pair of the transmits, such as (T_1, T_2) , (T_3, T_4) , \dots , (T_k, T_{k+1}) , \dots , (T_{M-1}, T_M) can be designed based on the two-transmit sequence. For example, both T_k and T_{k+1} consist of 8 cascaded waves with short time intervals. The 1st to 4th waves are tilted plane waves with a

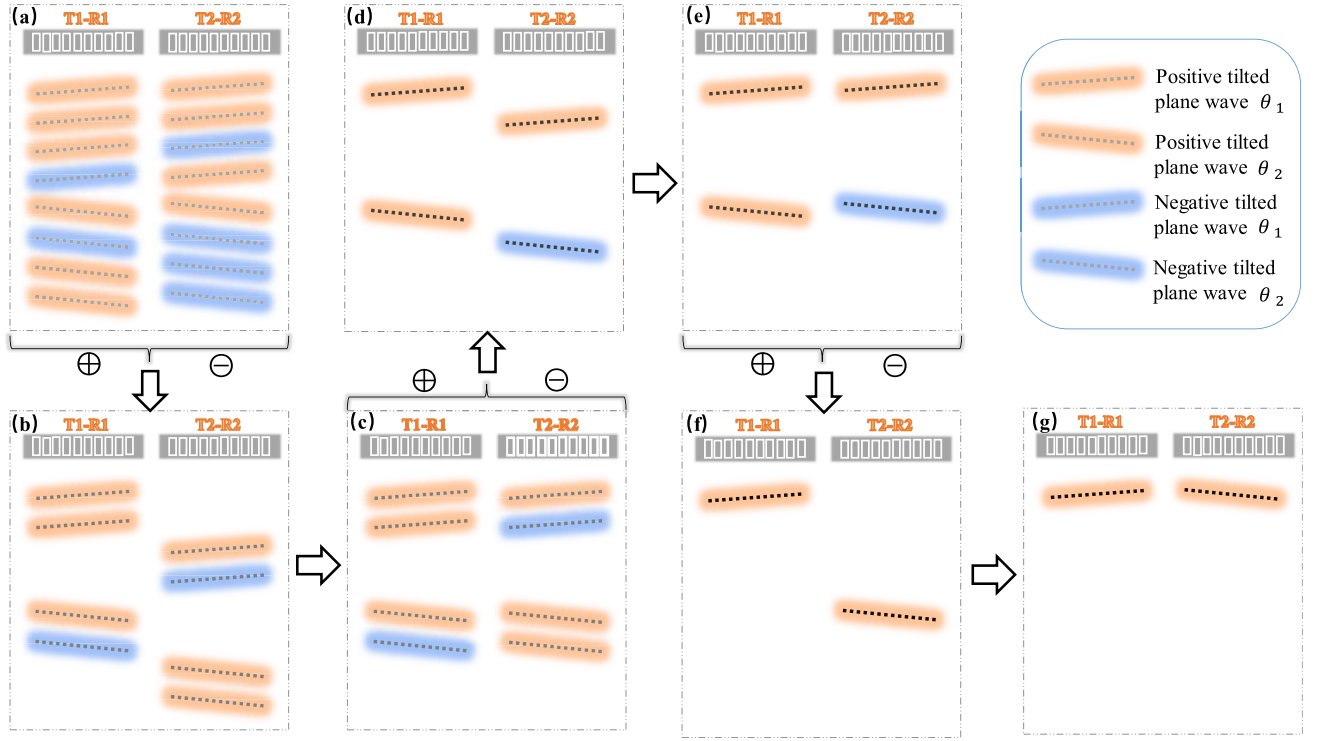


Fig. 4. Illustration of the 8 cascaded wave transmission sequence and reception decoding sequence design of our proposed CDW imaging.

steering angle of θ_k and the 5th to 8th waves are tilted plane waves with a steering angle of θ_{k+1} .

B. Application to Medical Ultrasound Imaging

The proposed CDW imaging sequence design was tested on point targets, a calibration phantom, *ex vivo* pork belly, and the *in vivo* human back muscle.

1) **Point Target Study:** The proposed CDW imaging sequence was first tested with a point target (nylon wires immersed in water) at 21.8 mm away from the array. The data were acquired using a Verasonics Vantage system (Verasonics, Kirkland, WA) equipped with a linear array transducer ATL L11-4v whose transmit center frequency was 8.9 MHz. Since ghost echoes exist in the received signals by full aperture plane waves and would obscure the illustration of the decoding process, the 64-th element, instead of full aperture, was active to transmit eight cascaded waves with an added 1.2 μ s short time interval. The polarity of each wave was obtained from the designed CDW matrix $C_{2 \times 8}$ in Section II-C. Full aperture was used in reception.

2) **B-Mode Imaging:** In medical ultrasound imaging, B-mode images are used to display the tissue anatomy. The CPWC, MW, and CDW sequences were successively performed to ensure the same scanning region for comparison. The two steered plane waves by the linear L11-4v probe (center frequency 8.9 MHz) with full aperture were at -2 degrees and 2 degrees. The base of the transmitted pulse was a short burst of one cycle. The azimuth of the image was from -19 mm to 19 mm. The compounded frame rate was 4000 fps. Sixteen cascaded waves with a 0.3 μ s short time interval were generated for each transmission event. In addition, CPWC and MW

imaging served as a reference. B-mode images were produced by the logarithmic compression of envelop detected data and displayed with grayscale colormap. The MI we used for the *ex vivo* and *in vivo* experiments was below 0.0814, which was calculated from hydrophone measurement of focused ultrasound beams in a degassed-water tank configuration. The experimental protocol of the back muscle was approved prior to use by the Institutional Review Board of the University of Hong Kong (UW 16-2012).

Quantitative evaluation metrics, such as spatial resolution, SNR, contrast ratio (CR), contrast to noise ratio (CNR), and penetration depth, were performed by 100 acquired images repeated with a fixed position of the imaging array probe from the phantom and *ex vivo* pork belly. Axial and lateral resolutions were calculated by the full width half maximum (FWHM) of the profile around the strong reflector at approximately 22 mm depth inside the calibration phantom. The calculation of SNR is the same as [32] and [35]. For each A-line at different depths, the ratios of the mean and the standard deviation of the 100 repeated acquisitions were calculated as an indication of SNR. The SNR represents the strength of sonographic signals over electric noise because the mean indicates the real signals, while the standard deviation represents the noise. The final SNR was obtained by the mean SNR among several A-lines as in [35] to increase the calculation robustness. The CR was calculated as $CR = |\mu_s - \mu_c|$, where μ_s and μ_c are the mean intensities of the regions of background and lesion/cyst, respectively. The CNR was calculated as $CNR = |\mu_s - \mu_c| / \sqrt{\sigma_s^2 + \sigma_c^2}$, where σ_s and σ_c are the intensity standard deviations of the background and lesion/cyst, respectively. The penetration depth was calculated

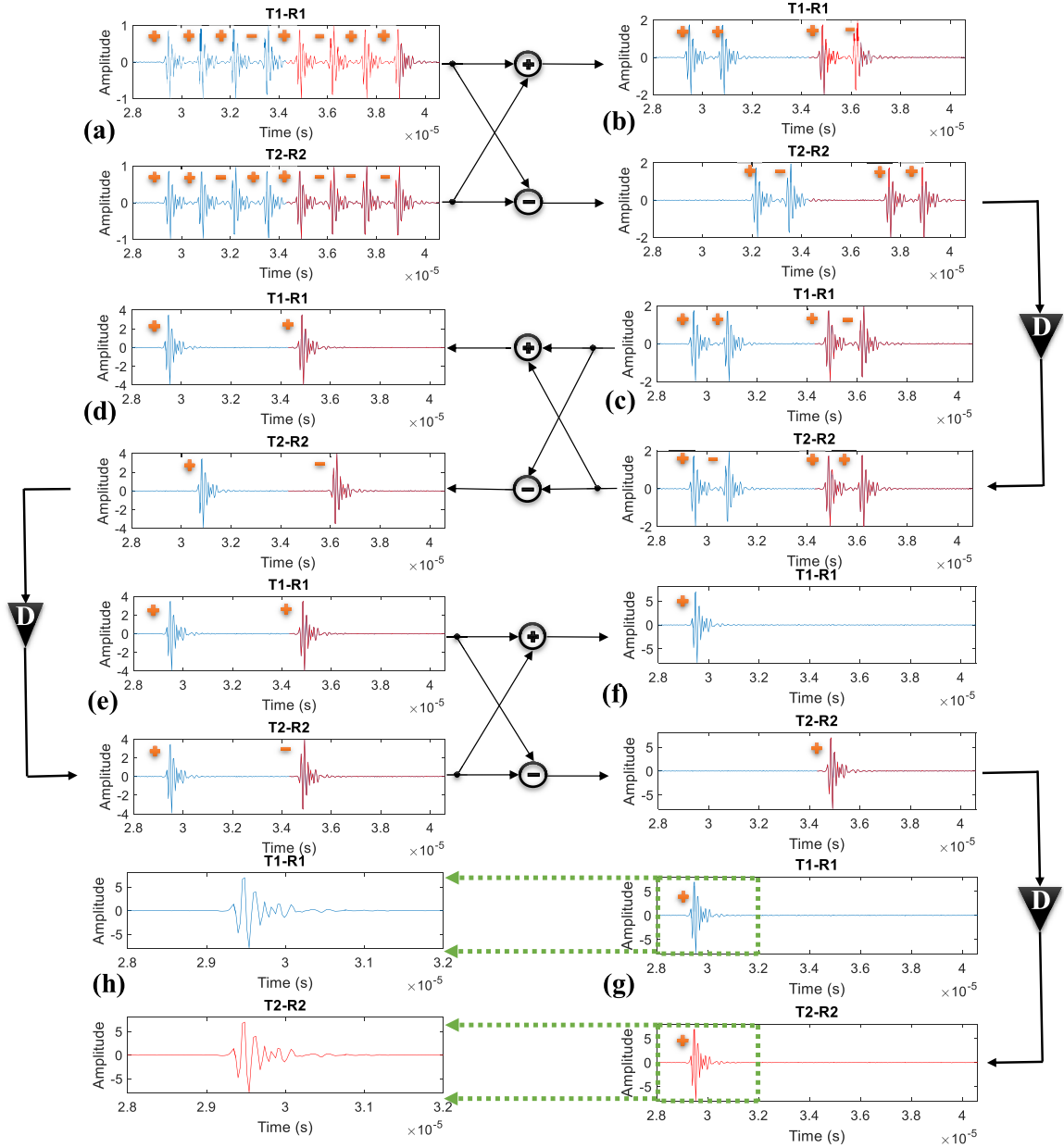


Fig. 5. Received signals from a wire phantom by two transmits with eight cascaded waves: (a) Initial received signals, (b)-(g) signals of each step in the decoding process, and (h) the recovered signals.

from the depth where SNR dropped to the minimum and then stabilized in the calibration phantom.

IV. RESULTS

A. Point Target Study

The received signals from a wire phantom using eight cascaded waves for each transmit event are shown in Fig. 5(a). The received signals have eight wavefronts with different polarity coefficients for each transmit event because each transmission is comprised of eight cascaded dual-polarity waves. The 1st to 4th waves are one type of wave (in blue color), and the 5th to 8th waves are another type of wave (in red color). The polarities of the wavefronts in the first and second receptions are $[+1, +1, +1, -1, +1, -1, +1, +1]$ and

$[+1, +1, -1, +1, +1, -1, -1, -1]$, respectively. They are the same as the designed CDW $C_{2 \times 8}$ matrix.

Figures 5(b)-(g) show the signals of each step of the decoding procedure. The aim of the decoding procedure is to separately recover the signals corresponding to the blue color and red color with an amplitude increase by eight fold. According to the decoding steps (1)-(6) in Section III-A, signals corresponding to the transmitted waves with blue color and red color were recovered as shown in Fig. 5(g) and Fig. 5(h), respectively. The amplitude of the recovered signal was eight-fold amplitude increase compared to the initially received signals in Fig. 5(a). Similarly, an N-fold amplitude increase can be obtained from N cascaded waves used for each transmission event.

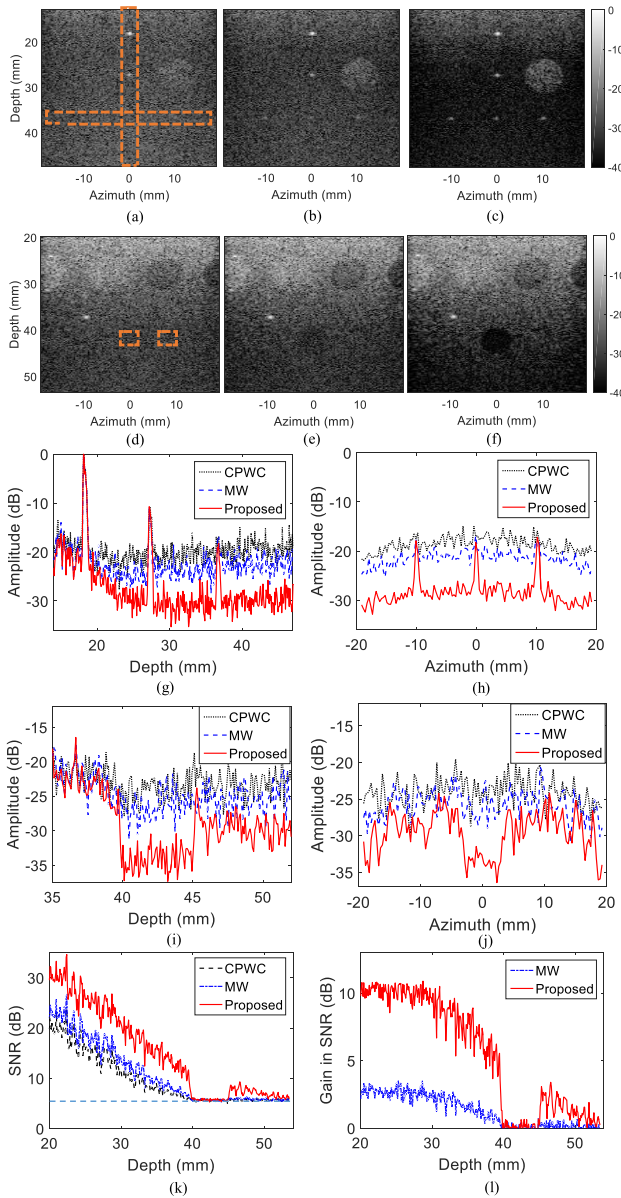


Fig. 6. B-mode images of a calibration phantom by CPWC (a, d), MW (b, e), and the proposed CDW (c, f) imaging. (a)-(c) show the point target regions, and (d)-(f) highlight a cyst region in a deep zone. (g) and (i) are axial profiles of the point target column (a-c) and the cyst (d-f), respectively, at azimuth 0 mm. (h) and (j) are lateral profiles of the point target row at depth 37.5 mm and the cyst at depth 42.5 mm, respectively. (k) shows SNR along the imaging depth at azimuth 0 mm of (d-f). (l) shows the gain in SNR with respect to CPWC at azimuth 0 mm of (d-f).

B. Calibration Phantom Study

Figure 6 shows the B-mode images, axial and lateral profiles, and SNR of the calibration phantom by CPWC, MW, and proposed CDW imaging. Figures 6(a)-(c) show that our proposed CDW imaging enabled increased penetration depth and the best delineation of the strong reflectors, especially at the depth of 37.5 mm. The axial profile (Fig. 6(g) and Fig. 6(j)) taken at azimuth 0 mm and the lateral profile (Fig. 6(h) and Fig. 6(k)) at imaging depth 37.5 mm (orange box in Fig. 6(a)) show that the suppression of the background noise level by CDW was approximately 10 dB more than that of CPWC

and 8 dB more than that of MW imaging. Figures 6(d)-(f) show that the proposed CDW imaging demonstrated the best delineation of the cyst at the depth of 42.5 mm. The axial profile at azimuth 0 mm in Fig. 6(i) and the lateral profile at the depth of 42.5 mm show the suppression of the noise level in the cyst by CDW was approximately 10 dB more than that of CPWC and 8 dB more than that of MW imaging. The SNR at azimuth 0 mm from Figs. 6(d)-(f) and Fig. 6(i) show that the SNR of CDW was much higher than that of CPWC and MW. The SNR gain evidenced in Fig. 6(l) shows that the SNR of the proposed CDW imaging was 10 dB and 7 dB higher than CPWC and MW imaging, respectively, in the near zone.

Table I shows the axial and lateral resolutions, CR, CNR, SNR, penetration depth, and the frame rate of CPWC, MW and CDW imaging. Axial and lateral resolutions were calculated at depth 18 mm and azimuth 0 mm from Figs. 6(a)-(c). Our proposed CDW imaging exhibited comparable spatial resolution to MW and CPWC but the lowest standard variation. CR and CNR were calculated at depth 42.5 mm and azimuth 0 mm from the region of interest (ROI) indicated in orange color in Fig. 6(d). The proposed CDW presented significant improvement of the CR and CNR compared with CPWC and MW imaging in deep regions. The improvement of CR by proposed CDW imaging was 5.97 dB as compared with CPWC and 5.05 dB as compared with MW imaging. The improvement of CNR by proposed CDW imaging was 0.85 dB as compared with CPWC and 0.70 dB as compared with MW imaging. The SNR value was selected from the central depth at 26.48 mm in Fig. 6(i). The improvement of SNR by the proposed CDW imaging was 10.71 dB as compared with CPWC and 7.62 dB as compared with MW imaging. The penetration depth was calculated from the depth where SNR dropped to the minimum and remained around 6 dB as indicated by the blue dotted line in Fig. 6(k). The improvement of the penetration depth by proposed CDW imaging was 36.94% as compared with CPWC and 35.14% as compared with MW imaging.

C. Ex Vivo Pork Belly Imaging

Figure 7 shows the B-mode images and SNR of *ex vivo* pork belly by CPWC, MW, and proposed CDW imaging. Figures 7(a)-(c) show that the proposed CDW imaging enabled comparable delineation of the muscle fibers in the ROI shallower than 30 mm depth. However, CDW enabled enhanced delineation (i.e., much higher clarity and continuity) of the muscle fibers in deep regions especially at the depths from 42 mm to 52 mm. Figure 7(d) shows that CDW exhibited much higher SNR at azimuth 0 mm than CPWC and MW. The gain of SNR in Fig. 7(e) shows that proposed CDW imaging increased around 10 dB in SNR compared with CPWC and 7 dB compared with MW imaging in the near zone.

D. In Vivo Human Back Muscle Imaging

Figure 8 shows the B-mode images of *in vivo* human back muscle by CPWC, MW, and proposed CDW imaging. Figures 8(a)-(c) show that the proposed CDW imaging enabled comparable delineation of the back muscle fibers in the ROI

TABLE I
COMPARISONS OF RESOLUTION, CONTRAST, SNR, PENETRATION AND FRAME RATE

Symbol	CPWC	MW	Proposed CDW	Proposed CDW compared to CPWC	Proposed CDW compared to MW
Axial resolution (mm)	0.45±0.028	0.43±0.015	0.43±0.006	(+ 4.4 %)	(+ 0 %)
Lateral resolution (mm)	0.54±0.018	0.53±0.011	0.53±0.005	(+ 1.9 %)	(+ 0 %)
CR (dB)	0.78±0.491	1.70±0.532	6.75±0.456	(+ 5.97)	(+ 5.05)
CNR (dB)	0.12±0.076	0.27±0.084	0.97±0.068	(+ 0.85)	(+ 0.70)
SNR (dB)	16.47	19.56	27.18	(+ 10.71)	(+ 7.62)
Penetration depth (mm)	38.98	39.50	53.38	(+ 36.94 %)	(+ 35.14 %)
Frame rate (fps)	4000	4000	4000	(+ 0 %)	(+ 0 %)

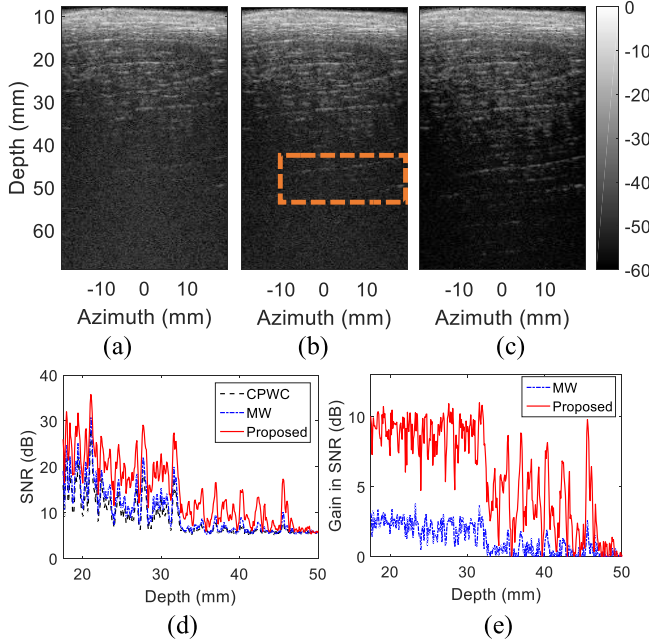


Fig. 7. B-mode images of *ex vivo* pork belly (a) CPWC, (b) MW, and (c) proposed CDW imaging. (d) SNR of along the axial direction at azimuth 0 mm, and (e) the gain of SNR along the axial direction.

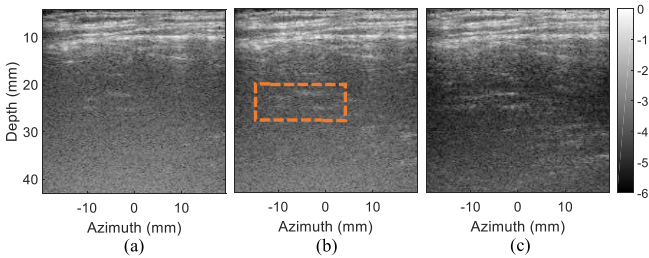


Fig. 8. B-mode images of *in vivo* human back muscle (a) CPWC, (b) MW, and (c) proposed CDW imaging.

shallower than 20 mm in depth. However, CDW enabled enhanced delineation of the structures in deep regions especially at depths from 20 mm to 28 mm.

V. DISCUSSION

In this study, a new ultrafast imaging methodology was proposed, coined as the cascaded dual-polarity wave (CDW) imaging. The proposed CDW imaging as evaluated in a point target, a calibration phantom, *ex vivo* pork belly, and *in vivo*

human back muscle showed significant improvement in SNR (10.71 dB vs. CPWC, 7.62 dB vs. MW), penetration depth (36.94 % vs. CPWC, 35.14% vs. MW), and CR (5.97 dB vs. CPWC, 5.05 dB vs. MW) in the scenario of ultrafast biomedical ultrasound imaging without compromising the frame rate and spatial resolution. The application of the CDW scheme in ultrafast ultrasound imaging is based on the transmission of cascaded short time interval waves with different amplitude coefficients from the newly designed CDW code matrix. By a simple decoding process with additions, subtractions, and delay operations, received signals were obtained as if emitted by the conventional single wave model but with increased amplitude. High sonographic SNR images can be reconstructed from the high SNR decoded received signals. Improvement of the penetration and image contrast in deep regions originates from the improvement of the SNR of the CDW-reconstructed B-mode images. Although the axial resolution (CPWC: 0.45 mm, MW: 0.43 mm, CDW: 0.43 mm) and lateral resolution (CPWC: 0.54 mm, MW: 0.53 mm, CDW: 0.53 mm) remain, it can be improved by the use of higher frequency ultrasound waves because higher SNR can compensate the higher attenuation, collectively producing B-mode images with better spatial resolution and contrast in both near zones and deep regions. Even though the number of transmits in CDW imaging should be even, the frame rate is the same as that of the CPWC and MW imaging.

We compared the performance of CDW with CPWC and MW imaging. The improvement of SNR and image contrast in deep regions by CDW depends on the number of transmitted cascaded waves for each transmit and has successfully been tested with as large as 16 waves for two compounded transmissions. The number of transmitted cascaded waves for each transmission-reception event can be any value of 2^k theoretically, which is much more flexible and larger than the two waves by MW imaging with the Hadamard matrix of order 2 for two compounded transmissions. In addition, the CDW can be applied to an even number of compounded transmission-reception events, making CDW much more flexible than MW imaging with 2^k transmission-reception events. For example, for $M \neq 2^k$ transmission events ($M = 6, 10, 12, 14, 18, \dots$), the designed CDW matrix can be applied for every two successive transmits, while MW imaging cannot work because the length of Hadamard matrix should be 2^k . The images of *ex vivo* pork belly by CDW imaging with four transmits ($M = 4$, steered plane waves with $-4, -2, 2, 4$

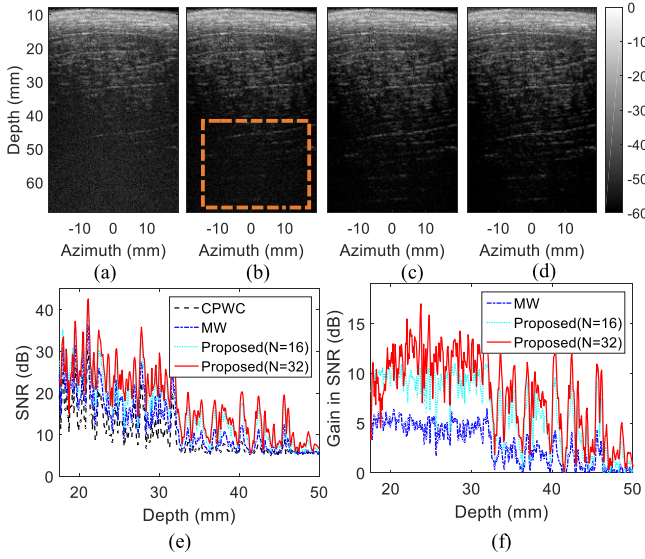


Fig. 9. B-mode images of *ex vivo* pork belly meat with four compounded transmits (four steered angles) (a) CPWC, (b) MW, (c) proposed CDW imaging with $N = 16$, and (d) proposed CDW imaging with $N = 32$. (e) SNR along the axial direction at azimuth 0 mm, and (f) the gain of SNR compared with CPWC along axial direction.

degrees, compounded frame rate is 2000 fps) and as large as 32 cascaded waves (0.3us short time interval) for each transmit were compared with CPWC and MW imaging as shown in Fig. 9. Note that the difference between Fig. 9 and Fig. 7 is the number of compounded transmits. Figs. 9(a)-(d) show that proposed CDW imaging ($N = 16$ and $N = 32$) offered enhanced delineation of the muscle fibers, especially in deep regions depths from 40 mm to 60 mm. The SNR at azimuth 0 mm in Fig. 9(e) shows that CDW exhibited much higher SNR than that of CPWC and MW. The SNR gain in Fig. 9(f) shows that proposed CDW imaging could increase SNR by around 10 dB with $N = 16$ and by around 13 dB with $N = 32$.

Similar to the MW imaging, CDW imaging with N cascaded waves for each transmission-reception event is equivalent to averaging or accumulating the received signals N times by CPWC in terms of SNR. However, the advantage of CDW imaging is that it does not compromise the frame rate for the same SNR, while the average or accumulation of data by CPWC is done at the expense of the frame rate by $1/N$, which is not preferred in ultrafast imaging. Assuming a white electronic noise in the acquired signals, the SNR gain would, in theory, be $10 \cdot \log_{10}(N)$ on the energy by CDW with N cascaded waves compared with CPWC. Experimental results from the calibration phantom and *ex vivo* pork belly in Fig. 6, Fig. 7, and Fig. 9 show that the increase of SNR was around 10 dB for 16 cascaded waves and 13 dB for 32 cascaded waves, which were slightly lower than that of the theoretical value with 12 dB for 16 waves and 15 dB for 32 waves. One possible reason is that the experimental noise or the variation of the reconstructed data among the 100 acquired images was not perfectly white noise. Another reason is the imperfect cancellation of the received positive pulse and negative pulse in the decoding process because of the second harmonic signals.

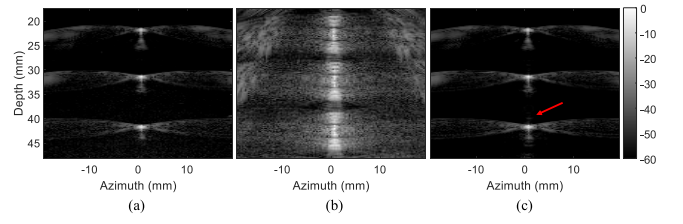


Fig. 10. B-mode images of a wire phantom by (a) CPWC, (b) CDW without decoding, and (c) proposed CDW imaging with decoding process. The red arrow indicates the weak artifacts caused by the imperfect decoding process.

For pulse-echo ultrasound imaging, the mechanical disruption of tissues due to cavitation as quantified by MI is proportional to the transmitted pulse voltage, and the maximum allowable MI limits the maximum amplitude of the transmitted signals. By using N cascaded waves with an allowed transmitted voltage in CDW imaging, the increase of SNR is equivalent to a \sqrt{N} -fold virtual increase of the transmitted amplitude of the single wave model in CPWC. Because of the underlying principle of the proposed CDW imaging, the spatial resolution was comparable to the CPWC and MW imaging but with higher CR and CNR in deep regions as shown in Fig. 6 and Table I. The contrast was improved in CDW imaging because the electronic noise was dominant over the axial and side lobe artifacts in deep regions. The decoding process was implemented on the initially received signals before the beamforming process. In our study, the addition, subtraction, and delay operations in the decoding process were directly implemented based on the received signals. The received signals of the array by each transmit-reception event was a two-dimensional (2D) matrix with N_s rows and 128 columns, where N_s was the number of samples of the received signal by each element and 128 was the number of array elements (see Section III-A). The computational cost mainly depends on the size of the 2D matrix. If the beamforming process is a linear process (i.e. delay and sum), the decoding process can also be implemented on the beamformed signals. In this case, the computational cost is also primarily determined by the size of the beamformed signals. In general, the size of the beamformed signals can be larger, smaller, or equal to the size of the initially received signals (i.e., channel data), and the corresponding computational cost varies with the size of beamformed signals. However, if the beamforming process is nonlinear (i.e. coherence-based beamforming), the decoding process cannot be implemented on the beamformed signals because the beamforming process changes the relationship of the signals between two transmit-reception events. Thus, it is better that we implement the decoding process on the initially received signals before the beamforming process; this is the same as other coded excitation techniques.

However, several limitations remain in CDW imaging. One limitation is the possible imperfect cancellation of the positive pulse and negative pulse. Because of the nonlinear propagation of the ultrasonic signals, the second harmonic signals of the positive and negative pulses cannot be canceled in the addition-operation step and will cause the range lobes as in the MW

imaging. This kind of effect can be suppressed by applying a 90% FIR bandwidth filter for the reception [32], [35]. Another factor causing imperfect cancellation of the positive and negative pulses is the motion effect as in the MW imaging. Since the decoding process needs two adjacent transmission-reception events, the movement of the scatterers between the two transmission-reception events will cause misalignment of the two received signals and thus the imperfect decoding of the received signals. However, the motion effect can be minimized because the ultrafast frame rate leads to a short time interval between two adjacent frames. The imperfect cancellation of the positive and negative pulses in the decoding process will cause the artifacts in the images. Figure 10 shows the B-mode images of a wire phantom by CPWC, CDW imaging without decoding process, and CDW imaging with decoding process in order to illustrate the performance of the decoding process. The parameters were the same as B-mode imaging in Section III-B. Apparent artifacts can be observed in the images by CDW without decoding process (Fig. 10b). Nevertheless, the point spread function of CDW imaging is comparable to that of CPWC (Fig. 10a) except weak artifacts indicated by the red arrow (Fig. 10c). However, the artifacts caused by the imperfect decoding process is much smaller than the original axial and lateral artifacts in CPWC. Another limitation is the dead zone in the near field due to the longer transmitted signals. The range of the dead zone is half the length of the transmitted long pulses. In our current settings, the duration of a single pulse is 0.11 μ s, and the short time interval between two pulses is 0.3 μ s. The durations of the 16 and 32 cascaded waves are therefore approximately 6.26 μ s and 12.52 μ s, respectively. Suppose that the speed of sound is 1540 m/s, the range of the dead zone is estimated to be around 4.82 mm for 16 cascaded waves and 9.64 mm for 32 cascaded waves. However, in deep region imaging, the region of interest is where SNR is initially low and generally beyond the dead zone. Since longer pulses need to be transmitted, the proposed CDW imaging method does not increase the MI but the Thermal Index (TI), which indicates the amount of tissue heating by ultrasound absorption. The longer the transmitted cascaded waves, the larger the TI. However, the MI limit is generally the dominant constraint for B-mode pulse-echo ultrasound imaging. The use of longer cascaded waves at similar voltage is permitted provided that the TI is below the FDA limit.

In addition, the type of wave used in this study is the plane wave. As discussed in Section III-A, the diverging and focused waves are also compatible with the CDW imaging. The evaluation of the CDW imaging with diverging wave and focused wave will be a future work. The *in vivo* demonstration of the proposed method was in the back muscle. The evaluation of the CDW imaging for other organs, such as the liver and kidney, will be in future work. In this study, B-mode images were the target for CDW assessment. Since the improvement of SNR can highly improve the estimation of tissue displacement and the sensitivity of power doppler imaging, the application of CDW imaging to ultrasound strain imaging, shear wave elastography, and ultrafast doppler imaging is propitious and will be investigated in our future work.

VI. CONCLUSIONS

A new ultrafast imaging methodology with cascaded dual-polarity waves (CDW) was proposed and applied in medical ultrasound imaging. The proposed CDW consists of a pulse train with newly designed positive and negative polarities. The proposed ultrafast ultrasound imaging with CDW outperforms current ultrafast imaging methods, such as CPWC and MW imaging, in terms of sonographic SNR (improvement 10.71 dB vs. CPWC, 7.62 dB vs. MW), penetration depth (improvement 36.94 % vs. CPWC, 35.14% vs. MW) and contrast in deep regions (improvement 5.97 dB vs. CPWC, 5.05 dB vs. MW) without compromising the frame rate and spatial resolution. CDW shows great potential for the deep tissue imaging and the same region of interest (ROI) with much higher ultrasound frequencies to obtain the improved image quality. Ongoing work includes the application of CDW in shear wave elasticity imaging and ultrafast Doppler imaging.

REFERENCES

- [1] M. Tanter and M. Fink, "Ultrafast imaging in biomedical ultrasound," *IEEE Trans. Ultrason., Ferroelect., Freq. Control*, vol. 61, no. 1, pp. 102–119, Jan. 2014.
- [2] T. Defieux, G. Montaldo, M. Tanter, and M. Fink, "Shear wave spectroscopy for *in vivo* quantification of human soft tissues visco-elasticity," *IEEE Trans. Med. Imag.*, vol. 28, no. 3, pp. 313–322, Mar. 2009.
- [3] P. Song, M. W. Urban, A. Manduca, H. Zhao, J. F. Greenleaf, and S. Chen, "Comb-push ultrasound shear elastography (CUSE) with various ultrasound push beams," *IEEE Trans. Med. Imag.*, vol. 32, no. 8, pp. 1435–1447, Aug. 2013.
- [4] W.-N. Lee *et al.*, "Mapping myocardial fiber orientation using echocardiography-based shear wave imaging," *IEEE Trans. Med. Imag.*, vol. 31, no. 3, pp. 554–562, Mar. 2012.
- [5] Y. Guo, H. Y. Lo, and W.-N. Lee, "Transmural transverse stiffness estimation in vascular shear wave imaging: A simulation and phantom study," *Appl. Phys. Lett.*, vol. 110, no. 19, p. 193701, 2017.
- [6] B. F. Osmanski, M. Pernot, G. Montaldo, A. Bel, E. Messas, and M. Tanter, "Ultrafast Doppler imaging of blood flow dynamics in the myocardium," *IEEE Trans. Med. Imag.*, vol. 31, no. 8, pp. 1661–1668, Aug. 2012.
- [7] E. Macé, G. Montaldo, I. Cohen, M. Baulac, M. Fink, and M. Tanter, "Functional ultrasound imaging of the brain," *Nature Methods*, vol. 8, no. 8, pp. 662–664, 2011.
- [8] J. Bercoff *et al.*, "Ultrafast compound Doppler imaging: Providing full blood flow characterization," *IEEE Trans. Ultrason., Ferroelect., Freq. Control*, vol. 58, no. 1, pp. 134–147, Jan. 2011.
- [9] C. Errico, B.-F. Osmanski, S. Pezet, O. Couture, Z. Lenkei, and M. Tanter, "Transcranial functional ultrasound imaging of the brain using microbubble-enhanced ultrasensitive Doppler," *NeuroImage*, vol. 124, pp. 752–761, Jan. 2016.
- [10] J. R. Lindner, "Molecular imaging of cardiovascular disease with contrast-enhanced ultrasonography," *Nature Rev. Cardiol.*, vol. 6, no. 7, pp. 475–481, 2009.
- [11] H. Li, Y. Guo, and W.-N. Lee, "Systematic performance evaluation of a cross-correlation-based ultrasound strain imaging method," *Ultrasound Med. Biol.*, vol. 42, no. 10, pp. 2436–2456, 2016.
- [12] C. Papadacci, E. A. Bunting, and E. E. Konofagou, "3D quasi-static ultrasound elastography with plane wave *in vivo*," *IEEE Trans. Med. Imag.*, vol. 36, no. 2, pp. 357–365, Feb. 2017.
- [13] J. Grondin, M. Waase, A. Gambhir, E. Bunting, V. Sargsyan, and E. E. Konofagou, "Evaluation of coronary artery disease using myocardial elastography with diverging wave imaging: Validation against myocardial perfusion imaging and coronary angiography," *Ultrasound Med. Biol.*, vol. 43, no. 5, pp. 893–902, 2017.
- [14] X. Yu, Y. Guo, S.-M. Huang, M.-L. Li, and W.-N. Lee, "Beamforming effects on generalized Nakagami imaging," *Phys. Med. Biol.*, vol. 60, no. 19, p. 7513, 2015.
- [15] L. Sandrin, S. Catheline, M. Tanter, X. Hennequin, and M. Fink, "Time-resolved pulsed elastography with ultrafast ultrasonic imaging," *Ultrason. Imag.*, vol. 21, no. 4, pp. 259–272, 1999.

- [16] J.-Y. Lu, "2D and 3D high frame rate imaging with limited diffraction beams," *IEEE Trans. Ultrason., Ferroelect., Freq. Control*, vol. 44, no. 4, pp. 839–856, Jul. 1997.
- [17] J. Cheng and J.-Y. Lu, "Extended high-frame rate imaging method with limited-diffraction beams," *IEEE Trans. Ultrason., Ferroelect., Freq. Control*, vol. 53, no. 5, pp. 880–899, May 2006.
- [18] G. Montaldo, M. Tanter, J. Bercoff, N. Benech, and M. Fink, "Coherent plane-wave compounding for very high frame rate ultrasonography and transient elastography," *IEEE Trans. Ultrason., Ferroelect., Freq. Control*, vol. 56, no. 3, pp. 489–506, Mar. 2009.
- [19] B. Denarie *et al.*, "Coherent plane wave compounding for very high frame rate ultrasonography of rapidly moving targets," *IEEE Trans. Med. Imag.*, vol. 32, no. 7, pp. 1265–1276, Jul. 2013.
- [20] H. Hasegawa and H. Kanai, "High-frame-rate echocardiography using diverging transmit beams and parallel receive beamforming," *J. Med. Ultrason.*, vol. 38, no. 3, pp. 129–140, 2011.
- [21] J. Porée, D. Posada, A. Hodzic, F. Tournoux, G. Cloutier, and D. Garcia, "High-frame-rate echocardiography using coherent compounding with Doppler-based motion-compensation," *IEEE Trans. Med. Imag.*, vol. 35, no. 7, pp. 1647–1657, Jul. 2016.
- [22] C. Papadacci, M. Pernot, M. Couade, M. Fink, and M. Tanter, "High-contrast ultrafast imaging of the heart," *IEEE Trans. Ultrason., Ferroelect., Freq. Control*, vol. 61, no. 2, pp. 288–301, Feb. 2014.
- [23] L. Tong, A. Ramalli, R. Jasaityte, P. Tortoli, and J. D'hooge, "Multi-transmit beam forming for fast cardiac imaging—Experimental validation and *in vivo* application," *IEEE Trans. Med. Imag.*, vol. 33, no. 6, pp. 1205–1219, Jun. 2014.
- [24] Y. Zhang, Y. Guo, and W.-N. Lee, "Ultrafast ultrasound imaging using combined transmissions with cross-coherence-based reconstruction," *IEEE Trans. Med. Imag.*, to be published, doi: [10.1109/TMI.2017.2736423](https://doi.org/10.1109/TMI.2017.2736423).
- [25] T. Misaridis and J. A. Jensen, "Use of modulated excitation signals in medical ultrasound. Part III: High frame rate imaging," *IEEE Trans. Ultrason., Ferroelect., Freq. Control*, vol. 52, no. 2, pp. 208–219, Feb. 2005.
- [26] T. Misaridis and J. A. Jensen, "Use of modulated excitation signals in medical ultrasound. Part II: Design and performance for medical imaging applications," *IEEE Trans. Ultrason., Ferroelect., Freq. Control*, vol. 52, no. 2, pp. 192–207, Feb. 2005.
- [27] A. Ramalli, F. Guidi, E. Boni, and P. Tortoli, "A real-time chirp-coded imaging system with tissue attenuation compensation," *Ultrasonics*, vol. 60, pp. 65–75, Jul. 2015.
- [28] T. Misaridis and J. A. Jensen, "Use of modulated excitation signals in medical ultrasound. Part I: Basic concepts and expected benefits," *IEEE Trans. Ultrason., Ferroelect., Freq. Control*, vol. 52, no. 2, pp. 177–191, Feb. 2005.
- [29] P. Song, M. W. Urban, A. Manduca, J. F. Greenleaf, and S. Chen, "Coded excitation plane wave imaging for shear wave motion detection," *IEEE Trans. Ultrason., Ferroelect., Freq. Control*, vol. 62, no. 7, pp. 1356–1372, Jul. 2015.
- [30] K. L. Gammelmark and J. A. Jensen, "Multielement synthetic transmit aperture imaging using temporal encoding," *IEEE Trans. Med. Imag.*, vol. 22, no. 4, pp. 552–563, Apr. 2003.
- [31] L. Demi, J. Viti, L. Kusters, F. Guidi, P. Tortoli, and M. Mischi, "Implementation of parallel transmit beamforming using orthogonal frequency division multiplexing—achievable resolution and interbeam interference," *IEEE Trans. Ultrason., Ferroelect., Freq. Control*, vol. 60, no. 11, pp. 2310–2320, Nov. 2013.
- [32] E. Tiran *et al.*, "Multiplane wave imaging increases signal-to-noise ratio in ultrafast ultrasound imaging," *Phys. Med. Biol.*, vol. 60, no. 21, p. 8549, 2015.
- [33] P. Gong, P. Song, and S. Chen, "Delay-encoded harmonic imaging (DE-HI) in multiplane-wave compounding," *IEEE Trans. Med. Imag.*, vol. 36, no. 4, pp. 952–959, Apr. 2017.
- [34] K. J. Horadam, *Hadamard Matrices and Their Applications*. Princeton, NJ, USA: Princeton Univ. Press, 2012.
- [35] P. Gong, P. Song, and S. Chen, "Ultrafast synthetic transmit aperture imaging using Hadamard-encoded virtual sources with overlapping sub-apertures," *IEEE Trans. Med. Imag.*, vol. 36, no. 6, pp. 1372–1381, Jun. 2017.